

Relation between the transmission rates and the wave functions in the carbon nanotube junctions

Ryo Tamura and Masaru Tsukada

Department of Physics, Graduate School of Science, University of Tokyo, Hongo 7-3-1, Bunkyo-ku, Tokyo 113, Japan

Electron transmission and wave functions through junctions with a pair of a pentagonal defect and a heptagonal defect connecting two metallic carbon nanotubes are analyzed by the analytical calculation with the effective mass equation. The energy region $|E| < E_c$ is considered where the channel number is kept to two. Close relation between the transmission rate and the wave function is found; the transmission rate is given by the inverse squared absolute value of the wave function. The dependence of the transmission rates on the energy and on the size of the junction is clearly explained by the nature of the wave function. Though the wave function and the transmission rate calculated by the tight binding model agree well with the corresponding analytical results by the effective mass approximation, the discrepancy becomes considerable when $|E| \simeq E_c$. To study the origin of this discrepancy, an efficient numerical calculation method is developed with a generalized transfer matrix for the tight binding model. Their numerical results are compared with the corresponding analytical ones and the results show that the origin of the discrepancy comes from the evanescent waves with the longest decay length in the tube parts.

72.80.Rj,72.10.Fk,73.50.-h,72.10.-d

I. INTRODUCTION

Recent experimental development on the carbon nanotubes, especially electronic transport measurements for individual nanotubes,¹ has promoted much interest in the nanotubes as one-dimensional conductor with nanometer size.² Many experimental works concern the theoretical prediction that the nanotube becomes metallic or semiconducting according to its circumference.^{3,4} The conductance of the metallic nanotubes with potential energy disorder has been studied.^{5,6} The junction structures with a shape of a part of a cone connecting two nanotubes with different radii have been also observed,⁷ and studied theoretically.⁸⁻¹¹ They are formed by a pair of a pentagonal defect and a heptagonal defect.¹²⁻¹⁴ By composing the nanotube junctions, the electronic circuits with nanometer size might be designed. The atom bond network of the nanotube junctions is uniquely determined by its development map with the vector of the circumference of the connected thicker nanotube \vec{R}_5 and that of the connected thinner tube \vec{R}_7 . We have calculated the conductance with Landauer's formula, i.e., the transmission rate, for the various junctions connecting two metallic nanotubes by the tight binding model.^{8,9} Surprisingly, the dependence of the transmission rate on the parameters, \vec{R}_5 , \vec{R}_7 and E , has a very simple form obeying the scaling law; in the energy region $|E| < E_c$ where the channel number is kept to two in both the tubes, the transmission rate is independent of detailed atomic arrangements as well as the angle between the two tube axes but determined only by the two parameters; one of the two parameters is the ratio of the circumference of the tubes R_7/R_5 and the other is the scaled energy E/E_c . The close relation between the transmission rate and the wave function in the junction part is also found by the tight binding model.^{8,9} When $E = 0$, the transmission rate decays with the thickness of the junction as $4/(2 + (R_5/R_7)^3 + (R_7/R_5)^3)$ while the spatial decay of the corresponding wave function in the junction part obeys the same power law.⁸ When $R_7/R_5 \simeq 0.5$, the transmission rate shows a peak structure as a function of the energy, while the corresponding wave function shows a resonant feature, i.e., its amplitude is enhanced in the middle of the junction part.⁹

Recently, Matsumura and Ando have confirmed the power law decay for $E = 0$ by using the effective mass theory.¹⁵ We generalized their discussion to more general energy region $|E| < E_c$, and obtained the complete analytical form of the transmission rate with the two parameters, R_7/R_5 and $|E|/E_c$.¹⁶ The agreement of the analytical transmission rate with the numerical one is found to be fairly good so far as $|E|$ is not very close to E_c . By our generalization of the effective mass approximation, the band structures of the periodic multiple nanotube junctions, which are called the 'helically coiled nanotube' in Ref.¹⁷, can be also obtained as closed analytical forms and their relation to the configuration of the pentagon and the heptagon are clearly explained based on the symmetry features.¹⁸ The effective mass theory is derived from the tight binding model and is valid when the energy is near zero. It is suitable to obtain the analytical results and to explain the origin of the scaling law because it treats not the discrete space but the continuous space, i.e., it does not necessitate the detailed atomic structures of the honeycomb lattice.^{6,15,16,18-20} Though the analytical transmission rate of the nanotube junction by the effective mass theory has been studied in detail in this way, the close relation between the transmission rate and the wave function observed in the numerical

result is not clarified by the effective mass theory yet. In this paper, the spatial variations of the wave function is expressed unambiguously by the effective mass theory and it gives an intuitive explanation for the dependence of the transmission rate on R_7/R_5 . Furthermore it will be also found that its dependence on the energy has close relation to the other parameter $|E|/E_c$ of the scaling law. These points are discussed in section III. The concise expression of the wave function characterized by only the two parameters will be useful when the STM images of the nanotube junction are analyzed.

On the other hand, the discrepancy between the numerical transmission rate with the tight binding theory and the analytical one by the effective mass approximation become considerable when $|E|$ is very close to E_c ; the numerical transmission rate shows a sharp dip there while the analytical one does not show. Since the effective mass theory is an approximation derived from the tight binding model, the numerical result by the tight binding model is considered to be correct one. To discuss the origin of the sharp dip, the wave functions calculated by the tight binding model have to be compared with those calculated by the effective mass theory. To calculate the wave function by the tight binding model more efficiently, a new numerical method is developed in section II. From the comparison of the wave function calculated by the method in section II with the analytical one, we found in section IV that the evanescent waves in the tube parts and the defect levels at the pentagon and the heptagon have important roles to form the dip structures.

II. THE CONDITIONED TRANSFER MATRIX METHOD

Fig.1 shows the development map of the nanotube junction. It is characterized by bars representing zig-zag segments of the C-C bond network in the circumferential direction of the single junction. They are aligned and numbered along the direction $\vec{e}_1 - \vec{e}_2$ where \vec{e}_1 and \vec{e}_2 are the basic translation vectors of the graphite plane. Each bar is connected with adjacent bars by the remaining C-C bonds. The network is rolled up so that the atoms denoted by j in the bottom of the j 'th bar and the top one of the same bar denoted by j' become the identical one. The j and j' sites are shown by the filled and the open circles in Fig.1, respectively. When $j \leq 0$, the j 'th bar is formed by the $(m+n)$ unit cells of the 2D graphite, where the m unit cells are aligned along \vec{e}_1 and the others are aligned along \vec{e}_2 . So the (m, n) tube defined in Ref.⁴ is formed there. When $1 \leq j \leq l_1$, the j 'th bar is defined as such that made by adding $(j-1)$ unit cells and one atoms along the direction of \vec{e}_1 to the bottom of the zeroth bar. For $j \geq l_1 + 1$, j 'th bar is made from the l_1 'th bar by exchanging $(l_2 - 1)$ unit cells and one atoms in its bottom aligned along \vec{e}_1 with l_2 unit cells aligned along \vec{e}_2 . The network made in this way represents the junction of the (m, n) tube ($j \leq 0$) and the (m_2, n_2) tube ($j \geq l_1 + 1$), where $l_1 = (m_2 + n_2) - (m + n) \geq 0$ and $l_2 = n_2 - n \geq 0$. This junction is called an (m, n) - (m_2, n_2) junction hereafter. Then Fig.1 corresponds to the (2,2)-(2,5) junction. A 7-membered ring is formed at the bottom of the 1st bar and a 5-membered ring is introduced between the l_1 'th bar and the $(l_1 + 1)$ 'th bar. There are only 6 membered rings elsewhere.

The number of the bonds connecting the $(j-1)$ 'th bar and the j 'th bar is denoted by b_j as

$$\begin{aligned} b_j &= m + n \quad (j \leq 0) \\ b_j &= m + n + j - 1 \quad (1 \leq j \leq l_1) \\ b_j &= m_2 + n_2 \quad (l_1 + 1 \leq j) \end{aligned} \quad (1)$$

The amplitudes of the wave function in the j 'th bar are represented by the vector $\vec{c}_j = {}^t (c_{j,1}, c_{j,2}, \dots)$. Its component $c_{j,i}$ can be classified to the two groups according to whether the corresponding site connect with the right $(j+1)$ 'th bar or with the left $(j-1)$ 'th bar. These two groups are denoted by r_j and l_j , respectively, as is shown in Fig.2. Since each site in j 'th bar belongs to only and necessarily one of the two groups, the dimension of \vec{c}_j equals $b_j + b_{j+1}$, which are denoted by d_j hereafter. The bonds between the $(j-1)$ 'th bar and the j 'th bar are numbered as Fig.2 from the bottom to the top. According to this way of numbering, the amplitudes are also numbered by $r_{j-1,i}$ and $l_{j,i}$, which have the bond numbered by i ($i = 1, 2, \dots, b_j$). Then the tight binding equation become

$$Er_{j-1,i} = \gamma(l_{j,i} + \sum_{i'} c_{j-1,i'}) \quad (2)$$

and

$$El_{j,i} = \gamma(r_{j-1,i} + \sum_{i''} c_{j,i''}) \quad (3)$$

where the first and the other terms in the right hand sides represent the bonds between the neighboring bars and those within the bar, respectively. Here we use the tight binding model including only π orbitals with common hopping

integral, $\gamma(\simeq -2.7\text{eV})$, and common site energy chosen to be zero. In order to get more accurate results, the effects from the mixing with σ orbitals caused by curvature of the graphitic plane also have to be considered. But we believe that this tight binding model gives a transparent view about this system and qualitative valid results. Another reason why this model is used is that the purpose of this paper is to focus on the effects from the *connectivity* of the bond network rather than those from the curvature.

The tight binding equation, eqs. (2) and (3) can be summarized by the matrix form as

$$A_j \vec{c}_{j-1} + B_j \vec{c}_j = 0 \quad , \quad (4)$$

where A_j and B_j are a $2b_j \times d_j$ matrix and a $2b_j \times d_{j+1}$ matrix, respectively. In the left (right) tube parts, i.e., when $j \leq 0$ ($j \geq l_1 + 2$), these matrixes become constant matrixes, A_L and B_L (A_R and B_R). The transfer matrixes for the tube parts are obtained as $T_L = -A_L^{-1}B_L$ for the left tube and $T_R = -A_R^{-1}B_R$ for the right tube. The eigen values and eigen vectors of T_μ are classified into two groups as $\{\beta_i^\mu, \psi_{+i}^\mu\}$ and $\{1/\beta_i^\mu, \psi_{-i}^\mu\}$. Hereafter, $\mu = R$ and $\mu = L$ represent the left thinner tube and the right thicker tube, respectively. The propagating waves in the former group, which are ψ_{+i} with $|\beta_i| = 1$, are assigned to $i = 1, \dots, n_\mu$, where n_μ is called the channel number of the corresponding tube. They carry the probability flow with the positive velocity, v_i . The propagating waves in the latter group, $\psi_{-i} = \psi_i^*$, carry that with the negative velocity, $-v_i$. From now on, the normalized extended states with unit flow, $\tilde{\psi}_i = \psi_i/\sqrt{v_i}$ and $\tilde{\psi}_{-i} = \psi_{-i}/\sqrt{v_i}$ are used instead of ψ_i and ψ_{-i} . The other states for $|i| > n_\mu$ are evanescent waves and the sign of i means the direction along which they decay exponentially, i.e., $|\beta_i^\mu| < 1$.

The wave function in the tube parts are represented by superposition of these eigen vectors and its coefficients are represented by \vec{x} as

$$\vec{c}_j = U_+^\mu (\Lambda^\mu)^{+j} \vec{x}_+^\mu + U_-^\mu (\Lambda^\mu)^{-j} \vec{x}_-^\mu \quad , \quad (5)$$

where the i 'th column of U_\pm^μ is the normalized eigen vector $\tilde{\psi}_\pm^\mu$, and Λ^μ is the diagonal matrix whose (i, i) element is the eigen value β_i^μ .

Unlike the tube parts, the 'usual' square transfer matrix cannot be obtained in the junction part, because the dimension of \vec{c}_j and that of \vec{c}_{j+1} are different, i.e., the A_j for $1 \leq j \leq l_1$ becomes a rectangle matrix which has no inverse matrix. Nevertheless there is a $d_{j-1} \times 2b_j$ matrix which is similar to the inverse matrix of A_j . It is denoted by \tilde{A}_j and defined by

$$\tilde{A}_j \equiv (A_j^\dagger A_j)^{-1} A_j^\dagger \quad . \quad (6)$$

This matrix satisfies the condition $\tilde{A}_j A_j = 1$ but $A_j \tilde{A}_j \neq 1$. By this pseudo-inverse matrix, we can define the 'transfer matrix', $T_j \equiv -\tilde{A}_j B_j$. If eq.(4) is satisfied, then

$$\vec{c}_{j-1} = T_j \vec{c}_j \quad (7)$$

is satisfied, but its converse does not hold generally. It means that \vec{c}_{j+1} in eq.(7) cannot be chosen to be arbitrary but has to satisfy

$$(B_j + A_j T_j) \vec{c}_j = 0 \quad . \quad (8)$$

To make eq.(7) equivalent to eq.(4), the condition (8) is necessary, so we call T_j a 'conditioned transfer matrix' hereafter. In our problem, the number of the independent rows of $(B_j + A_j T_j)$ is only one, so eq.(8) can be written as

$${}^t \vec{s}_j \cdot \vec{c}_j = 0 \quad , \quad (9)$$

where ${}^t \vec{s}_j$ is one of the nonzero rows of $(B_j + A_j T_j)$. Multiplying T_j generates the coefficient at the bar with the decreased j , so we define the positive direction along which j decreases, i.e., from the right thicker tube to the left thinner tube.

By using the inverse matrix ${}^t ({}^t V_+^L, {}^t V_-^L) \equiv (U_+^L, U_-^L)^{-1}$ and $K_j \equiv T_j T_{j+1} \cdots T_{l_1}$, the relation between \vec{c}_{l_1+1} and the right going waves in the thinner tube \vec{x}_-^L are summarized as

$$\begin{pmatrix} V_-^L K_0 \\ {}^t \vec{s}_{l_1+1} \\ {}^t \vec{s}_{l_1} K_{l_1} \\ {}^t \vec{s}_{l_1-1} K_{l_1-1} \\ \vdots \\ {}^t \vec{s}_2 K_2 \end{pmatrix} \vec{c}_{l_1+1} = \begin{pmatrix} \vec{x}_-^L \\ 0 \\ 0 \\ 0 \\ \vdots \\ 0 \end{pmatrix} \quad . \quad (10)$$

The $(m_2 + n_2) \times (2m_2 + 2n_2)$ matrix in the left hand side of eq.(10) is represented by Q hereafter.

Now we define all the necessary things to calculate the transmission rate and the wave function. When the electron is incident from the right and transmitted into the thinner tube, i.e., when $\vec{x}_+^R \neq 0$ and $\vec{x}_-^L = 0$, the reflected wave \vec{x}_-^R and the transmitted wave \vec{x}_+^L are obtained from

$$\vec{x}_-^R = -(QU_-^R)^{-1}(QU_+^R)\vec{x}_+^R \quad (11)$$

and

$$\vec{x}_+^L = V_+^L K_0 (U_+^R - U_-^R (QU_-^R)^{-1} (QU_+^R)) \vec{x}_+^R, \quad (12)$$

respectively. The corresponding wave function in the junction part, i.e., \vec{c}_j for $1 \leq j \leq l_1$ is given by

$$\vec{c}_j = K_j (U_+^R - U_-^R (QU_-^R)^{-1} (QU_+^R)) \vec{x}_+^R. \quad (13)$$

For the inverse direction of the incident electron, $\vec{x}_+^R = 0$ and $\vec{x}_-^L \neq 0$, the reflected wave \vec{x}_+^L and the transmitted wave \vec{x}_-^R are obtained from

$$\vec{x}_+^L = V_+^L K_0 U_-^R (QU_-^R)^{-1} \begin{pmatrix} \vec{x}_-^L \\ 0 \end{pmatrix}, \quad (14)$$

and

$$\vec{x}_-^R = (QU_-^R)^{-1} \begin{pmatrix} \vec{x}_-^L \\ 0 \end{pmatrix}. \quad (15)$$

In this case, the wave function in the junction part is given by

$$\vec{c}_j = K_j U_-^R (QU_-^R)^{-1} \begin{pmatrix} \vec{x}_-^L \\ 0 \end{pmatrix}. \quad (16)$$

The transmission rate is obtained from eq.(12) or eq.(15), while the reflection rate is obtained from eq.(11) or eq.(14) from the matrix elements corresponding to the open channel, i.e., $x_{\pm i}^\mu$ with $i = 1 \sim n_\mu$. We have confirmed that unitarity holds very well in the conditioned transfer matrix method. Agreement of their results with those calculated by usual recursive Green's function methods is also quite good. In both the methods, matrix inversions are necessary about l_1 times, but they can be done much faster in the conditioned transfer matrix method than in the recursive Green's function method, because matrixes which have to be inverted are real sparse symmetric matrixes, $A_j^\dagger A_j$, in the former method while those in the latter method are complex matrixes with no symmetry. Therefore the 'conditioned transfer matrix' method is much faster than the recursive Green's function method. This efficiency is expected to be more important when more general related problems are calculated, e.g., those including electron-phonon interaction or electron-electron interaction self-consistently. Another advantage of the conditioned transfer matrix method over the recursive Green's function method, which is not essential but practically important, is that it is more intuitive and easy to be implemented.

In section IV, the wave functions are calculated numerically by the conditioned transfer matrix method and compared to those calculated analytically by the effective mass equation.

III. EFFECTIVE MASS THEORY AND ITS APPLICATION TO THE SINGLE NANOTUBE JUNCTION

Fig. 3 shows a development map of the nanotube junction neglecting the atomic sites. The vectors \vec{R}_5 and \vec{R}_7 represent the circumferences of the thicker tube and the thinner tube, respectively. Lines $E_7 P_7 P_5 E_5$ and lines $F_7 Q_7 Q_5 F_5$ are stucked each other so that the points connected by \vec{R}_j become identical ($j = 5, 7$). Then $P_5 (= Q_5)$ and $P_7 (= Q_7)$ turn out to be the centers of a heptagonal defect and a pentagonal defect, respectively. These points are marked also in Fig.1. Thus from now on, the indices '7' and '5' are used to represent the thinner and the thicker tube, respectively.

The equilateral triangles ' $\Delta O P_7 Q_7$ ' and ' $\Delta O P_5 Q_5$ ' with bases ' $P_7 Q_7$ ' and ' $P_5 Q_5$ ' have a common apex O , which is chosen to be the origin of the coordinate (x, y) in this paper.¹⁰ The origin O lies between $-(m+n)$ 'th bar and $-(m+n-1)$ 'th bar, since $\vec{Q}_7 O = m\vec{e}_2 + n(\vec{e}_2 - \vec{e}_1)$.

Then the position of a general site, \vec{r} , can be labeled by (s, q_1, q_2) , where q_1 and q_2 are integer components representing the position of the unit cell, $\vec{q} \equiv q_1 \vec{e}_1 + q_2 \vec{e}_2$, and s represents the sublattice, $s = A, B$. Relation between the position vector of the site, \vec{r} , and its label (s, q_1, q_2) is written by

$$\begin{aligned}\vec{r}(A, q_1, q_2) &= \vec{q} + (\vec{e}_1 + \vec{e}_2)/3 \\ &= \frac{\sqrt{3}}{2}(q_1 + q_2 + \frac{2}{3})\vec{e}_x + \frac{1}{2}(q_2 - q_1)\vec{e}_y\end{aligned}\quad (17)$$

and

$$\begin{aligned}\vec{r}(B, q_1, q_2) &= \vec{q} + 2(\vec{e}_1 + \vec{e}_2)/3 \\ &= \frac{\sqrt{3}}{2}(q_1 + q_2 + \frac{4}{3})\vec{e}_x + \frac{1}{2}(q_2 - q_1)\vec{e}_y.\end{aligned}\quad (18)$$

In the above $\vec{e}_x \equiv (\vec{e}_1 + \vec{e}_2)/\sqrt{3}$ and $\vec{e}_y \equiv \vec{e}_2 - \vec{e}_1$, which define the coordinate system (x, y) shown in Fig.1. The amplitude of the wave function at these sites is denoted by $\psi(s, q_1, q_2)$. In the effective mass theory, the wave function is represented by

$$\psi(s, q_1, q_2) = F_s^K(\vec{r})w^{(q_1 - q_2)} + F_s^{K'}(\vec{r})w^{(q_2 - q_1)} \quad (s = A, B). \quad (19)$$

Here $w \equiv \exp(i2\pi/3)$ and \vec{r} is defined by eqs.(17) and (18) as a function of the label (s, q_1, q_2) . In eq.(19), $F_{A,B}^{K,K'}$, $w^{(q_1 - q_2)}$ and $w^{(q_2 - q_1)}$ are the envelop wave functions, the wave function of the Bloch states at the K and the K' point, respectively. This wave function is expressed by a vector, $\vec{\psi} = (F_A^K(\vec{r}), F_B^K(\vec{r} + \vec{e}_x/\sqrt{3}), F_A^{K'}(\vec{r}), F_B^{K'}(\vec{r} + \vec{e}_x/\sqrt{3}))$, hereafter. This definition of F 's is different from other references^{6,16,19,15} by certain factors. The reason why this definition is used is that the representation of the time reversal operation I , $I\psi = \psi^*$, becomes simpler as

$$I(F_A^K, F_B^K, F_A^{K'}, F_B^{K'}) = ((F_A^{K'})^*, (F_B^{K'})^*, (F_A^K)^*, (F_B^K)^*) . \quad (20)$$

By using eq.(19), the effective mass equation are derived from the tight binding equation used in the preceding section. When energy E is zero, $w^{q_1 - q_2}$ and $w^{q_2 - q_1}$ are solutions of the tight binding model, so that the corresponding solutions of the envelop functions F are constant. Thus when E is not zero but close to zero, spatial variation of the envelop functions is slow compared to the lattice constant, $|\vec{e}_x| = |\vec{e}_y| \equiv a \simeq 0.25\text{nm}$. In this case, it is a good approximation to take only the first order term in the Taylor expansion of the envelop function as $F(\vec{r} + \vec{e}_x) \simeq (1 + a\partial_x)F(\vec{r})$. From this approximation, one obtains^{6,19,20}

$$(-i\partial_y + \partial_x)F_B^K(\vec{r} + \vec{b}) = \epsilon F_A^K(\vec{r}) \quad (21)$$

$$(-i\partial_y - \partial_x)F_A^K(\vec{r}) = \epsilon F_B^K(\vec{r} + \vec{b}) . \quad (22)$$

$$(i\partial_y + \partial_x)F_B^{K'}(\vec{r} + \vec{b}) = \epsilon F_A^{K'}(\vec{r}) \quad (23)$$

$$(i\partial_y - \partial_x)F_A^{K'}(\vec{r}) = \epsilon F_B^{K'}(\vec{r} + \vec{b}) , \quad (24)$$

where $\epsilon = 2E/(\sqrt{3}\gamma a)$ and $\vec{b} \equiv \vec{e}_x/\sqrt{3}$. When the plane wave solution $F_A^K, F_B^K \propto \exp(\pm i\vec{k} \cdot \vec{r})$ is used in eqs.(21) and (22), one can get linear isotropic dispersion relation,

$$k \equiv |\vec{k}| = |\epsilon| , \quad (25)$$

and $F_B^K(\vec{r} + \vec{b})/F_A^K(\vec{r}) = \pm \exp(i\eta)$, where $(k_x, k_y) = (-\epsilon \sin \eta, \epsilon \cos \eta)$, i.e., η is the angle of \vec{k} with respect to the y axis measured anti-clockwise. It follows that the corresponding wave function, $\vec{\psi}_{K\pm}$, is written as

$$\vec{\psi}_{K\pm} = (e^{-i\eta/2}, \pm e^{i\eta/2}, 0, 0)e^{\pm i(\vec{k} \cdot \vec{r})} . \quad (26)$$

The wave number must satisfy the boundary condition in the metallic nanotube parts as

$$\vec{k} \cdot \vec{R}_j = 2\pi l_j \quad (j = 5, 7) , \quad (27)$$

where l_j is an integer representing the number of oscillations of the envelop function around the circumferences. As for the semiconducting tubes, the boundary condition becomes different from eq.(27)¹⁹, but we concentrate our discussion to the metallic nanotubes in this paper. The upper sign and the lower sign in eq.(26) represent the direction of the propagating waves. When E is close to zero, i.e., $k \simeq 0$, only possible number of l_j is zero. It means that \vec{k} is perpendicular to \vec{R}_j so that η is the angle of \vec{R}_j with respect to x axis. Within the effective mass theory scheme, the possible maximum value of l_5 (l_7) is the channel number of the thicker tube (the thinner tube). Therefore the range of the energy where the channel number is kept to two in the thicker tube (the thinner tube) is $|E/\gamma| < \sqrt{3}\pi a/R_5$ ($|E/\gamma| < \sqrt{3}\pi a/R_7$). Discussions in this paper are concentrated to the energy region where the channel number is kept to two in both the tubes. It is represented by $|E| < (\sqrt{3}\pi|\gamma|)(a/R_5) \equiv E_c$ and E_c is called a threshold energy hereafter. From the propagating waves near the K point, $\vec{\psi}_{K\pm}$, the other propagating waves $\psi_{K'\pm}$ are obtained by the time reversal operation (20) as

$$\vec{\psi}_{K'\pm} = I\vec{\psi}_{K\mp} = (0, 0, e^{i\eta/2}, \mp e^{-i\eta/2})e^{\pm i(\vec{k}\cdot\vec{r})} . \quad (28)$$

Note that the direction of the propagation is reversed by the time reversal operation I . In order to discuss the wave function in the junction part, the polar coordinate (r, θ) is useful. Its relation to the coordinate (x, y) is the usual one, i.e., $r = \sqrt{x^2 + y^2}$, $\tan \theta = y/x$. Then the wave function satisfies the wave equation $r^2(\partial_x^2 + \partial_y^2 + k^2)F = (z^2\partial_z^2 + z\partial_z + \partial_\theta^2 + z^2)F = 0$, where $z = kr$. The solution is represented by Bessel functions J_m and Neumann functions N_m as

$$F = \sum_{m=-\infty}^{\infty} e^{im\theta} (c_m J_{|m|}(z) + d_m N_{|m|}(z)) . \quad (29)$$

In Fig.1, site i is identical with site i' for $i = 1, \dots, l_1$, while corresponding labels (s, q_1, q_2) are different between i and i' ; that for i is $(B, 1, -4 - i)$ and that for i' is $(A, 3 + i, -2 - i)$. In this way, the wave function in the junction part must satisfy the condition

$$\psi(A, q_1, q_2) = \psi(B, q_1 + q_2, -q_1 - 1) . \quad (30)$$

Here transformation of the label $(A, q_1, q_2) \rightarrow (B, q_1 + q_2 + 1, -q_1 - 1)$ is equivalent to clock-wise rotation by $\pi/3$ with respect to the origin O . From eqs. (30) and (19), the boundary conditions in the junction part are derived as

$$F_A^{K'}(r, \theta + \pi/3) = w F_B^K(r, \theta) , \quad (31)$$

and

$$F_A^K(r, \theta + \pi/3) = \frac{1}{w} F_B^{K'}(r, \theta) . \quad (32)$$

The other boundary conditions

$$F_B^K(r, \theta + \pi/3) = w F_A^{K'}(r, \theta) , \quad (33)$$

and

$$F_B^{K'}(r, \theta + \pi/3) = \frac{1}{w} F_A^K(r, \theta) . \quad (34)$$

are also obtained in the same way. The same boundary conditions are firstly discussed by Matsumura and Ando.¹⁵ Difference of eqs. (31) - (34) from those of Matsumura and Ando by certain factors is due to the difference of the definition of $F_{A,B}^{K,K'}$. From eqs. (31) and (32), terms in eq. (29) for $F_A^{K'}$ and F_B^K are not zero only when $m = 3p + 2$ ($p = \text{integer}$). Because the open channel $l_j = 0$ in the tube parts is spatially uniform along the circumference, it is better fitted to the components with smaller $|m|$ in eq. (29) than to those with larger $|m|$. So we assume that one can neglect all the terms except those with $p = 0$ and $p = -1$ in eq. (29) (Assumption I). Then the wave functions can be written as

$$F_A^{K'} = e^{2i\theta} f_2(z) + e^{-i\theta} f_1(z), \quad (35)$$

and

$$F_B^K = e^{2i\theta} f_2(z) - e^{-i\theta} f_1(z) , \quad (36)$$

where

$$f_m(z) = c_m J_m(z) + d_m N_m(z) \quad (m = 1, 2). \quad (37)$$

From eqs. (21) and (24), the other two wave functions $F_B^{K'}$ and F_A^K can be derived from $F_A^{K'}$ and F_B^K as

$$F_B^{K'} = \frac{\epsilon}{|\epsilon|} \left(-e^{i\theta} \tilde{f}_2(z) + e^{-i2\theta} \tilde{f}_1(z) \right) , \quad (38)$$

$$F_A^K = \frac{\epsilon}{|\epsilon|} \left(e^{i\theta} \tilde{f}_2(z) + e^{-i2\theta} \tilde{f}_1(z) \right) , \quad (39)$$

where

$$\begin{aligned} \tilde{f}_1(z) &= c_1 J_2(z) + d_1 N_2(z), \\ \tilde{f}_2(z) &= c_2 J_1(z) + d_2 N_1(z) . \end{aligned} \quad (40)$$

In the above we used the recursion formula of the Bessel functions and Neumann functions.²¹ It is easily confirmed that eqs. (38) and (39) satisfy the boundary conditions eqs. (33) and (34). The amplitude of the open channel in the tube, which is denoted by α , is obtained from eq.(26) as

$$\alpha_{j\pm}^K = \frac{1}{2\sqrt{R_j}} \int_{Q_j}^{P_j} dx^{(j)} (e^{i\frac{\eta_j}{2}} F_A^K \pm e^{-i\frac{\eta_j}{2}} F_B^K) \quad (j = 5, 7) , \quad (41)$$

for the K point. The value of $|\alpha|^2$ equals the probability flow as shown in Appendix. The indices $+$ and $-$ mean the direction along which the electron waves propagate. The path of the integral of eq.(41) is the straight line $P_j Q_j$, the angle of which with respect to x axis is denoted by η_j . Equations for $\alpha_{j\pm}^{K'}$ are obtained from eq. (41) by replacing \pm , η_j and K in the r. h. s with \mp , $-\eta_j$ and K' , respectively. To simplify the calculation, the integrations in the above are transformed as

$$\int_{Q_j}^{P_j} dx^{(j)} \rightarrow R_j \int_{-\frac{2}{3}\pi + \eta_j}^{-\frac{\pi}{3} + \eta_j} d\theta . \quad (42)$$

If variation of the wave function along the radial directions is slow near $r = R_j$, this replacement can be allowed (Assumption II). The relation between the amplitudes of the open channel in each tube, $\vec{\alpha}_j = {}^t(\alpha_{j+}^K, \alpha_{j+}^{K'}, \alpha_{j-}^{K'}, \alpha_{j-}^K)$, and the coefficients representing the wave functions in the junction part, $\vec{g} = {}^t(c_2, d_2, c_1, d_1)$, are summarized in the followings.

$$\vec{\alpha}_j = \frac{1}{2} \sqrt{R_j} P(\eta_j) M \Lambda(\eta_j) L(kR_j) \vec{g} \equiv Y_j \vec{g} , \quad (43)$$

where M is a constant matrix given by²¹

$$M = \begin{pmatrix} -i\frac{\epsilon}{|\epsilon|} & 0 & 0 & -\frac{\sqrt{3}}{2}\frac{\epsilon}{|\epsilon|} \\ 0 & -\frac{\sqrt{3}}{2} & -i & 0 \\ 0 & -\frac{\sqrt{3}}{2} & i & 0 \\ i\frac{\epsilon}{|\epsilon|} & 0 & 0 & -\frac{\sqrt{3}}{2}\frac{\epsilon}{|\epsilon|} \end{pmatrix} . \quad (44)$$

$\Lambda(\eta)$ is a diagonal matrix, where $\Lambda_{1,1} = \Lambda_{3,3}^* = e^{i\eta}$ and $\Lambda_{2,2} = \Lambda_{4,4}^* = e^{2i\eta}$. $P(\eta)$ is defined by eq. (41) as

$$P(\eta) = \begin{pmatrix} e^{i\frac{\eta}{2}} & e^{-i\frac{\eta}{2}} & 0 & 0 \\ 0 & 0 & e^{-i\frac{\eta}{2}} & -e^{i\frac{\eta}{2}} \\ 0 & 0 & e^{-i\frac{\eta}{2}} & e^{i\frac{\eta}{2}} \\ e^{i\frac{\eta}{2}} & -e^{-i\frac{\eta}{2}} & 0 & 0 \end{pmatrix} . \quad (45)$$

The matrix elements of $L(z)$ are $L_{11} = L_{33} = J_1(z)$, $L_{12} = L_{34} = N_1(z)$, $L_{21} = L_{43} = J_2(z)$ and $L_{22} = L_{44} = N_2(z)$. The other matrix elements of $L(z)$ are zero. From eq. (43), the relation between $\vec{\alpha}_7$ and $\vec{\alpha}_5$ is given by $\vec{\alpha}_7 = Y_7 Y_5^{-1} \vec{\alpha}_5$ with the three parameters, kR_7 , kR_5 and $\phi \equiv \eta_7 - \eta_5$ (angle between \vec{R}_5 and \vec{R}_7 in the development map). This reads as

$$\begin{pmatrix} \vec{\alpha}_{7+} \\ \vec{\alpha}_{7-} \end{pmatrix} = \begin{pmatrix} t_1 & t_2^* \\ t_2 & t_1^* \end{pmatrix} \begin{pmatrix} \vec{\alpha}_{5+} \\ \vec{\alpha}_{5-} \end{pmatrix} . \quad (46)$$

where

$$t_1 = h_+ \begin{pmatrix} \cos(\frac{3}{2}\phi) & i \sin(\frac{3}{2}\phi) \\ i \sin(\frac{3}{2}\phi) & \cos(\frac{3}{2}\phi) \end{pmatrix} , \quad (47)$$

$$t_2 = h_- \begin{pmatrix} -\cos(\frac{3}{2}\phi) & -i \sin(\frac{3}{2}\phi) \\ i \sin(\frac{3}{2}\phi) & \cos(\frac{3}{2}\phi) \end{pmatrix} . \quad (48)$$

The factors h_+ and h_- in eqs.(47) and (48) are represented by

$$h_{\pm} = -\frac{1}{4} (X_{12}(kR_7, kR_5) \mp X_{21}(kR_7, kR_5)) + \frac{i}{2\sqrt{3}} \left(X_{11}(kR_7, kR_5) \pm \frac{3}{4} X_{22}(kR_7, kR_5) \right) \quad (49)$$

where

$$X_{i,j}(z_1, z_2) \equiv \sqrt{z_1 z_2} \pi \{ J_i(z_1) N_j(z_2) - N_i(z_1) J_j(z_2) \} . \quad (50)$$

The considered energy region $|E| < E_c$ corresponds to the region, $0 < kR_5 < 2\pi$. It can be easily confirmed analytically that eq. (46) satisfies the time reversal symmetry and unitarity. The transmission rate per channel denoted by T is calculated from eq.(46) as

$$T = 1/|h_+|^2 = \frac{2}{\{(1/6) \sum_{i=1}^2 \sum_{j=1}^2 (3/4)^{i+j-2} X_{i,j}^2(kR_5, kR_7)\} + 1} , \quad (51)$$

and it gives the conductance σ as $\sigma = 2T$ by Landauer's formula. In Fig. 4, the solid lines represent the values of T calculated by the tight binding model, and the dotted line and the dashed line represent those calculated by eq. (51). Agreement between the two methods is fairly good.¹⁶ When $E = 0$, T becomes

$$T = \frac{4}{(R_5/R_7)^3 + (R_7/R_5)^3 + 2} . \quad (52)$$

Eq. (52) reproduces well the numerical results in Reference.⁸

We are now ready to consider the analytical calculation of the wave functions by the effective mass theory and its relation to the transmission rate. Let us consider the case where the two waves $\vec{\alpha}_{5+}^{(i)}$ ($i = 1, 2$) are incident from the thicker tube, and there is no incidence from the thinner tube, i.e., $\vec{\alpha}_{7-} = 0$. As in section II, it is called the positive incidence direction. Whenever the two incident waves are 'orthogonal' and have the same flow,²² i.e., $|\vec{\alpha}_{5+}^{(1)}| = |\vec{\alpha}_{5+}^{(2)}|$ and $t_{\vec{\alpha}_{5+}^{(1)*}} \cdot \vec{\alpha}_{5+}^{(2)} = 0$, the corresponding two transmitted waves are also "orthogonal" and have the same flow, because $t_1^\dagger t_1 = 1/T$. Note that it does not hold generally and characteristic of the nanotube junction.^{23,24}

The two orthogonal transmitted waves are represented by $\vec{\alpha}_{7+}^{(1)} = {}^t(a_1, a_2)$ and $\vec{\alpha}_{7+}^{(2)} = {}^t(-a_2^*, a_1^*)$. In the analytical calculation, we use different normalization from that of section II; we take the transmitted waves with unit flow represented by $|\vec{\alpha}_{7+}^{(i)}| = 1$ in this section while the incident waves have unit flows, $|\vec{\alpha}_{5+}^{(i)}| = 1$, in section II. Corresponding wave functions denoted by $\psi^{(i)}$ are obtained from $\vec{g} = Y_7^{-1} \vec{\alpha}_7^{(i)}$ and eqs.(35)-(40). They depend on the phases of a_1 and a_2 , but the sum of the squared absolute values of them, $\Psi(s, q_1, q_2) \equiv |\psi^{(1)}(s, q_1, q_2)|^2 + |\psi^{(2)}(s, q_1, q_2)|^2$, does not depend on them and can be determined uniquely. Therefore we discuss $\Psi = |\psi^{(1)}|^2 + |\psi^{(2)}|^2$ rather than $|\psi^{(1)}|^2$ and $|\psi^{(2)}|^2$, hereafter. Similar discussions are also possible for the negative incidence direction. The $\Psi(s, q_1, q_2)$ in the junction part is derived as

$$\Psi(A, q_1, q_2) = \frac{1}{3r} \sum_{i=1}^2 (3/4)^{i-1} \left(X_{i,1}^2 + X_{i,2}^2 + 2 \frac{\epsilon}{|\epsilon|} \cos \left(\theta + \frac{2\pi}{3} (q_1 - q_2) \right) X_{i,1} X_{i,2} \right) , \quad (53)$$

and

$$\Psi(B, q_1, q_2) = \frac{1}{3r} \sum_{i=1}^2 (3/4)^{i-1} \left(X_{i,1}^2 + X_{i,2}^2 - 2 \frac{\epsilon}{|\epsilon|} \cos \left(\theta - \frac{2\pi}{3}(q_1 - q_2) \right) X_{i,1} X_{i,2} \right), \quad (54)$$

where $X_{i,j} = X_{i,j}(kR_t, kr)$ is defined by eq.(50), with the circumference R_t of the tube into which the electron is transmitted. That is to say, $R_t = R_7$ and $kR_t < kr < kR_5 < 2\pi$ for the positive incidence direction, while $R_t = R_5$ and $kR_7 < kr < kR_t < 2\pi$ for the negative incidence direction. Note that the squared wave function Ψ in eqs.(53) and (54) does depend on the sign of energy unlike the conductance in eq.(51). Note also that the sign of E is inverse of that of ϵ , $E/|E| = -\epsilon/|\epsilon| = \pm 1$, because the transfer integral γ is negative. In the right hand sides of eqs.(53) and (54), only the third term depends on the angle θ , and it becomes zero as E approaches zero, because $X_{i,i} \rightarrow 0$. Therefore the spatial oscillation of Ψ along the θ direction decreases with decreasing $|E|$.

There are several possible choice of the basic translation vectors, \vec{e}_1 and \vec{e}_2 . The wave function represented by eqs.(53) and (54) should be invariant under the change of the choice. When $\vec{e}'_1 = \vec{e}_2$ and $\vec{e}'_2 = \vec{e}_2 - \vec{e}_1$ are used instead of (\vec{e}_1, \vec{e}_2) , the corresponding x', y' axes are rotated ones by $\pi/3$ with respect to original x, y axes as shown in Fig.1. Correspondingly, the polar coordinates and the labels are transformed as $(r, \theta) \rightarrow (r, \theta - \pi/3)$, $(A, q_1, q_2) \rightarrow (B, q_1 + q_2, -q_1 - 1)$ and $(B, q_1, q_2) \rightarrow (A, q_1 + q_2 + 1, -q_1 - 1)$. For example, the site indicated by the square symbol near the origin O in Fig.1 has the two different labels, which are $(A, 0, 0)$ defined by (\vec{e}_1, \vec{e}_2) and $(B, 0, -1)$ defined by (\vec{e}'_1, \vec{e}'_2) . Under this transformation of (r, θ) and (s, q_1, q_2) , the values of eqs.(53) and (54) are invariant, that is to say, the results are independent of the way of the labeling, or choice of the vectors, \vec{e}_1 and \vec{e}_2 .

In order to relate the wave function to the transmission rate, the integral of the squared wave function defined below should be introduced:

$$\Phi(kR_t, kr) \equiv \frac{9r}{14\pi} \int_Q^P d\theta (\Psi(A; r, \theta) + \Psi(B; r, \theta)) = \frac{1}{7} \sum_{i=1}^2 \sum_{j=1}^2 (3/4)^{i-1} X_{i,j}^2(kR_t, kr). \quad (55)$$

The third terms in r. h. s of eqs.(53) and (54) do not contribute to the integral because $q_1 - q_2$ varies rapidly as a function of θ . We call Φ defined by eq.(55) a radial norm, hereafter. The radial norm is normalized so that it equals unity at $r = R_t$, i.e., at the exit of the transmitted wave from the junction part. It corresponds to the unit flow of the transmitted wave. Thus at the entrance of the incident wave into the junction part, the radial norm Φ becomes the sum of the amplitude of incident wave $1/T$ and that of the reflected wave $R/T = (1 - T)/T$. Accordingly, the transmission rate T can be given by $T = 2/(\Phi + 1)$, where $\Phi = \Phi(kR_7, kR_5)$ for the positive incidence direction and $\Phi = \Phi(kR_5, kR_7)$ for the negative incidence direction. Figure 5 is the schematic development maps representing this relation between the radial norm and the transmission rate. It shows two junctions with a common thicker tube where the incidence direction is negative. Though they have different transmission rates, T_1 and T_2 , their wave functions in the region CC'D'D and the transmitted wave are common. From now on, we call $2/(\Phi + 1)$ an 'inverse' of the radial norm for simplicity. The inverse of the radial norm, $2/(\Phi(kR_7, kR_5) + 1)$, $2/(\Phi(kR_5, kR_7) + 1)$ and the transmission rate T of eq.(51) are shown in Fig.6 as a function of E/E_c by the dashed lines, the dotted lines and the solid lines, respectively. The curves are shown for the cases $R_7/R_5 = 0.1, 0.3, 0.5, 0.7$ and 0.9 . For each value of R_7/R_5 , the inverse of the radial norm is close to the corresponding transmission rate. Therefore we can discuss the dependence of the transmission rate on R_7/R_5 and $|E|/E_c$ by the radial norm. For this purpose, we show in Fig.7 the radial norm for the negative incidence directions, $\Phi(kR_5, kr)$, as a function of r/R_5 at six energies $E/E_c = kR_5/(2\pi) = 0.1, 0.3, 0.5, 0.65, 0.8, 1.0$. There are four regions of the parameter space which have different characters; they are region I ($1 > r/R_5 > 0.9$; $1 > |E|/E_c \geq 0$), II ($0.9 > r/R_5 > 0.1$; $0.7 > |E|/E_c \geq 0$), III ($0.9 > r/R_5 > 0.1$; $1 > |E|/E_c > 0.7$) and IV ($0.1 > r/R_5 > 0$; $1 > |E|/E_c \geq 0$). In the region I, all the curves in Fig.7 are very close to unity. It indicates that the corresponding transmission rate is near unity and independent of $|E|/E_c$ as is shown by the lines of $R_7/R_5 = 0.9$ in Fig.6. In the region II, the radial norm shows monotonic decrease as either r/R_5 or $|E|/E_c$ increases. The decrease with respect to r/R_5 becomes steep as $|E|/E_c$ decreases and are almost proportional to $(R_5/r)^3$ when $|E|/E_c < 0.1$. In the region III, however, the radial norm oscillates as r/R_5 increases. When $|E|/E_c = 1$ the radial norm has a minimum value around $r/R_5 = 0.5$. Correspondingly, the curves of $R_7/R_5 = 0.5$ are larger than those of $R_7/R_5 = 0.3$ and 0.7 at $|E|/E_c = 1$ in Fig.6. It oscillates also with increasing $|E|/E_c$ when $0.4 > R_5 > 0.2$. The lines of $R_5/R_7 = 0.3$ in Fig.6 shows the corresponding oscillations. Around the boundary between the region II and III, the decrease of the radial norm with increasing r/R_5 becomes critical as is indicated by the plateau of the curve corresponding to $|E|/E_c = 0.65$ in Fig.7. Correspondingly, all the curves for $R_7/R_5 = 0.7, 0.5$ and 0.3 in Fig.6 cross each other around the boundary energy $E/E_c = 0.7$. In the region IV, the radial norm is nearly proportional to $(R_5/r)^3$ so that the transmission rate is almost proportional to $(R_7/R_5)^3$ at each value of $|E|/E_c$.

The oscillating behavior in the region III can be interpreted as a resonant effect in the following discussion. The wave function propagates both in the radial and the angular direction. Its wave length along the radial direction is assumed to be close to that of the plane wave obtained from the dispersion relation (25); the wave length is given by $2\pi/k = R_5|E_c/E|$. When the length of the junction part along the radial direction, i.e., $R_5 - R_7$, coincides with the half of the wave length, the resonance occurs. From this discussion, the condition of the resonance can be easily obtained as

$$R_7/R_5 = 1 - |E_c/2E| . \quad (56)$$

The minimum points of the curves in Fig.7 in the region III correspond to this resonance following approximately condition (56); it comes around $r/R_5 = 0.5$ when $|E|/E_c = 1$ and moves towards the left as $|E|/E_c$ decreases. Around the resonance point, the transmission is almost perfect. Such a resonance, however, does not occur in the region II and IV, since the radial norm becomes divergent when kr approaches zero, i.e., when either $|E|/E_c = kR_5/(2\pi)$ or r/R_5 approaches zero. This divergence comes from the terms of $krN_2^2(kr)$ in eq.(55) which is almost proportional to $1/(kr)^3$ for small kr values. Accordingly, the transmission rate decays with the power law in proportion to $(R_7/R_5)^3$ in the region II and IV.

IV. COMPARISON BETWEEN THE ANALYTICAL RESULTS AND THE NUMERICAL RESULTS

Since the effective mass theory is an approximation of the tight binding model as is explained in the section III, its results have to be confirmed by comparing them to the corresponding numerical results from the tight binding model. In this section, we shall compare the wave function calculated numerically by the tight binding model, \tilde{c}_j , with those determined analytically by eqs.(53) and (54), Ψ . For the numerical calculation with the tight binding model, the conditioned transfer matrix method explained in section II is used. Figure 8 shows the ratio of the corresponding quantities, $(|c_{j,i}^{(1)}|^2 + |c_{j,i}^{(2)}|^2)/(T\Psi)$ as a function of radial distance r , for the energy $E = -0.05|\gamma|$. The values are plotted for the (3,3)-(13,13) junction in Fig.8-(a) and for the (10,10)-(13,13) junction in Fig.8-(b). Here the incidence direction is positive; $c_{j,i}^{(k)}$ is caused by the incident waves $\tilde{\psi}_{+k}^R$. For the opposite incidence direction, similar results are also obtained. Here the factor $1/T = |h_+|^2$ defined by eq.(49) is necessary because the transmitted waves have unit flow in eqs.(53) and (54), while the incident waves have unit flow in eq.(13). One can see that the ratio is close to unit, i.e., the coincidence is fairly good. Correspondingly, the transmission rate by the conditioned transfer matrix and that by eq.(51) coincide well with each other when $|E| < 0.2|\gamma|$, as shown in Fig.4. The deviation from unity becomes smaller as $|E|$ approaches zero, because all the assumptions postulated in deriving eqs.(53) and (54) are more valid for smaller $|E|$. The deviations, however, become larger when $r \simeq R_5$ in Fig.8-(a), while such a feature is not found in Fig.8-(b). The most natural explanation for this difference is that the deviations are caused mainly by the evanescent waves in the tube parts, and their effects become more significant as their decay lengths along the tube axis become larger, i.e., as they approach the extended states. The decay length is determined by $l_{5,7}$ in eq.(27) as $a/\sqrt{(2\pi l_{5,7}a/R_{5,7})^2 - \epsilon^2}$. Thus the discussion below is concentrated to the most extended evanescent waves corresponding to $l_{5,7} = \pm 1$. When $R_5 \gg R_7$ as the case of Fig.8-(a), the evanescent waves in the thicker tube side are much more extended and have larger effects than those in the thinner tube side. As a result, the deviation near the thicker tube side is enhanced compared to that in the other place. On the other hand, when $R_5 \simeq R_7$ as the case of Fig.8-(b), the evanescent waves have similar decay lengths both in the thicker and in the thinner tube side, so that the difference of the deviation does not depend on the sides.

To see the spatial variation of the wave function, we show $|\tilde{c}_j|^2$ of the (3,3)-(13,13) junction calculated by the conditioned transfer matrix method and the corresponding quantities determined analytically by eqs.(53) and (54). The former is shown by the closed symbols joined by the dotted lines and the latter is shown by the open symbols joined by the solid lines for $E = \pm 0.2|\gamma|$ in Fig.9-(a) and for $E = \pm 0.23|\gamma|$ in Fig.9-(b). The horizontal axis is the number of the bar j , which are almost proportional to the radial distance r . The diamonds and the squares correspond to the positive energy and the negative energy, respectively. Fig.9-(a) shows that the results by the two methods agree quite well. Enhancement of the deviation at $j = 16 \sim 20$ is caused by the evanescent waves. In Fig.9-(a), the wave function does not show monotonic decrease along the incidence direction but has a peak structure. It gives rise to the resonant peak structures near $E = \pm 0.2|\gamma|$ in Fig.4 which is already discussed in the previous section. In contrast to the good agreement in Fig.9-(a), the deviation becomes quite large in Fig.9-(b) especially near $r = R_5$; the wave function by the conditioned transfer matrix grows more rapidly than that by the analytical results with approaching the thicker tube side. When $|E| \simeq E_c$, as in the case of Fig.9-(b), the decay lengths of the evanescent waves are very large, and cause the large discrepancies. Corresponding to it, large discrepancies occur also in the transmission rate; only the data by the tight binding model show the sharp dips near $E = \pm 0.23\gamma$ in Fig.4. The sharp dip appears

approximately when $0.9 \leq |E/E_c| \leq 1$, i.e., when the decay length of the evanescent waves in the thicker tube are larger than the diameter of the thicker tube. Evanescent waves with their decay length larger than the diameter of the corresponding tube are called 'quasi-extended' evanescent waves hereafter.

In Fig.8, data corresponding to sites belonging to the pentagonal defect or the heptagonal defect are shown by closed diamonds. They indicate that the numerical wave function calculated by the tight binding model is more localized at the defects than the analytical wave function. Hereafter a localization strength for the θ direction at the defect is defined as the ratio between the numerical norm per site at the defect and that of the bars the defect belongs to. It is calculated by the tight binding model and represented by $(\sum_{i,k \in C_7} |c_{0,i}|^2 + |c_{1,k}|^2)(d_0 + d_1)/(7|\bar{c}_0|^2 + 7|\bar{c}_1|^2)$ at the heptagon and $(\sum_{i,k \in C_5} |c_{l_1,i}|^2 + |c_{l_1+1,k}|^2)(d_{l_1} + d_{l_1+1})/(5|\bar{c}_{l_1}|^2 + 5|\bar{c}_{l_1+1}|^2)$ at the pentagon with the notation of section II. Here $i \in C_n$ means that site i belongs to the n membered ring defect. Since the radial distance r in the bar is almost constant, the analytical quantity corresponding to the localization strength has a maximum represented by $\sum_{i=1}^2 (|X_{i,1}| + |X_{i,2}|)^2 / \sum_{i=1}^2 (|X_{i,1}|^2 + |X_{i,2}|^2) \leq 2$ which is shown from eqs.(53) and (54). Therefore we can say that the wave function is 'quasi-localized' at the defect when the localization strength is larger than two. The localization strength at the pentagon and that at the heptagon are shown as a function of the energy in Fig.10-(a) and Fig.10-(b), respectively. The solid lines and the dashed lines show the localization strength for the the (10, 10)-(13, 13) junction and that for the (3, 3)-(13, 13) junction, respectively. The solid lines shows that the the wave function is quasi-localized at both the defects when $|E| \simeq E_c$ and $R_7/R_5 \simeq 1$, i.e., when there are quasi-evanescent waves in both the tubes. Furthermore they also show asymmetry with respect to the energy axis; the quasi-localization at the pentagon (at the heptagon) around $E = -E_c$ ($E = +E_c$) is larger than that around the energy with the opposite sign. These results indicate that the quasi-localization occurs due to the mixing between the quasi-extended evanescent waves and the 'defect levels'. Here the 'defect levels' are defined as n discrete energy levels, $-2|\gamma| \cos(2\pi l/n)$ ($l = 1, 2, \dots, n$), of an isolated n membered ring calculated by the tight binding model.¹³ Since the energy region around zero is considered now, the discrete level closest to $E = 0$, which is at $E \simeq -0.618|\gamma|$ for the pentagon, and at $E \simeq +0.445|\gamma|$ for the heptagon, is the most important. The closer distance in the energy between the two states enhances their mixing so that it causes the asymmetry with respect to the energy. Since the defect levels are caused by the discreteness of the lattice, these results can not be reproduced by the effective mass equation.

The energy where the quasi-localized evanescent waves in the thinner tube side appear is around $E = \pm E_c R_5/R_7$. When $R_7/R_5 \ll 1$, it is distant from the considered energy region $|E| < E_c$ so that there is no quasi-extended evanescent waves in the thinner tube side. Though there are the quasi-extended evanescent waves in the thicker tube side, the defect level of the heptagon cannot be mixed with them due to the large spatial distance between the heptagon and the thicker tube. This is the reason why the dashed line in Fig.10-(b) do not show the quasi-localization. In summary, we can say that the defect level is mixed with the quasi-extended evanescent waves only when they are close to each other both in the energy and in the space.

In this way, the analytical results by the effective mass approximation are not appropriate when the evanescent waves become quasi-extended. The width of this energy region, however, is only about $0.1E_c$. Except these narrow energy region, the analytical results are appropriate enough.

V. SUMMARY AND CONCLUSION

In this paper, the junctions connecting the two metallic nanotubes with different circumferences by a pair of the pentagonal and the heptagonal defect are investigated. Both the wave function and the transmission rate are analytically obtained by the effective mass equation, and a close relation between them is found. To discuss the close relation, the junction part is divided into pieces according to the radial distance r from the thinner tube side and the radial norm of the wave function is evaluated in each piece. The radial norm is determined by the two parameters, $|E|/E_c$ and r/R_5 where E_c and R_5 are the threshold energy and the circumference of the thicker tube, respectively. The transmission rate approximates to the inverse of the radial norm where r is substituted with the circumference of the thinner tube, R_7 . From the dependence of radial norm on the two parameters, the parameter space is roughly classified into the four regions; region I ($1 > r/R_5 > 0.9$; $1 > |E|/E_c \geq 0$), II ($0.9 > r/R_5 > 0.1$; $0.7 > |E|/E_c \geq 0$), III ($0.9 > r/R_5 > 0.1$; $1 > |E|/E_c > 0.7$) and IV ($0.1 > r/R_5 > 0$; $1 > |E|/E_c \geq 0$). In the region I, the radial norm is close to unity so that the corresponding transmission is almost perfect, independent of $|E|/E_c$. In the region III, the radial norm oscillates near unity as the function of either of the two parameters. The period of the oscillation with respect to r is approximately the same as half wave length. Here the wave length is that of the plane wave, i.e., it is obtained from the liner dispersion relation of the monolayer graphite, eq.(25). Almost perfect transmission due to the resonance occurs in region III when the radial length of the junction part, $R_5 - R_7$, coincides with this period, because the corresponding radial norm has a minimum value there. As either $|E|/E_c = kR_5/(2\pi)$ or r/R_5 decreases, however, the radial norm becomes divergent owing to the term $krN_2^2(kr)$ so that the corresponding transmission rate

approaches zero. It leads to the power law decay of the transmission rate proportional to $(R_7/R_5)^3$ in the region II and IV instead of the resonant feature.^{8,9,16}

The nanotube junction can be considered as a combined system, that is the quasi two-dimensional structure (= the junction part) connecting the two quasi one-dimensional structures (= the tube parts). The wave functions in the former part become the 2D waves, whose radial parts are given by the sum of $J_i(kr)$ and $N_i(kr)$ ($i = 1, 2$), while they are the 1D plane waves in the tube parts. Nevertheless, the condition of the resonance in the region III, eq.(56), is obtained from the wave length of the 1D plane wave. It indicates that the four components of the wave function in the junction part, $J_i(kr)$ and $N_i(kr)$ ($i = 1, 2$), are combined appropriately to be fitted well with the 1D plane waves in the tube parts. On the other hand, the wave function shows the power law decay along the radial direction in the region II and IV, because only the component $N_2(kr)$ becomes dominant. In other words, the wave function in the junction part has the two dimensional character in the region II and IV so that its matching with the plane wave in the tube parts becomes worse than in the region III. The wave function in the junction part has different dimensionalities in this way.

The wave functions analytically obtained by the effective mass equation are compared with that numerically obtained by the tight binding model. When $|E|$ is very close to E_c , the discrepancies between them becomes considerable. From the dependence of the discrepancies on the radial distance, we speculate that they are mainly due to the evanescent waves with their decay length larger than the diameter of the corresponding tube and they are called quasi-extended evanescent waves. The quasi-extended evanescent waves cause the sharp dip of the transmission rate, which is absent in the analytical result. When the quasi-extended evanescent waves and the energy levels of the n membered ring defect ($n = 5, 7$) are close both in the energy and in the space, mixing between them appears as the enhancement of the wave function at the corresponding defect. Nevertheless coincidence between the analytical wave functions and the numerical ones are fairly good except the narrow energy region $0.9 < |E/E_c| < 1$.

The nature of the wave function discussed in this paper can be observed by Scanning Tunneling Microscopy (STM), because STM images reflect the Local Density of States (LDOS), which are proportional to the sum of the squared wave functions, eqs. (53) and (54), in the nanotube junction part. The third terms in eqs. (53) and (54) give rise to the $\sqrt{3} \times \sqrt{3}$ pattern or the oscillation along the θ direction in the STM images. They fade away as $|E|$ approaches zero. It is also expected that the images depend on the direction of the electronic current 'along the tube axes', which should not be confused with that of the tunneling current 'from the STM tip to the sample'. When $R_5/R_7 \gg 1$ and $E \simeq 0$, for example, the squared absolute value of the wave function in the junction part is almost proportional to r^2 when the current flows from the thicker tube to the thinner tube and to $1/r^4$ when it flows along the inverse direction. We expect that these results will promote the investigation of the nanostructures composed by the nanotubes including the nanotube junctions.

ACKNOWLEDGMENT

This work is supported in part by the Core Research for Evolutional Science and Technology (CREST) of the Japan Science and Technology Corporation(JST).

APPENDIX

In the tight binding model, the probability flow from site i to site j is represented by $\text{Im}(a_i^* H_{i,j} a_j)$, where a_i is the amplitude of the wave function at site i and $H_{i,j}$ is the hopping integral connecting site i and j . Conservation of the flow is guaranteed by the tight binding equation, $E a_i = \sum_j H_{i,j} a_j$. In this paper, $H_{i,j}$ is nonzero only when i and j are nearest neighbors. Consider bars for $j \leq 0$ forming to the (m, n) nanotube part in Fig.1. The amplitudes of wave functions are represented by $r_{j,i}$ and $l_{j,i}$ in the same way as Fig.2. Then the flow between $j - 1$ 'th bar and j 'th bar is represented by $\gamma \sum_{i=1}^{m+n} \text{Im}(r_{j-1,i}^* l_{j,i})$. Hereafter the common hopping integral between the nearest neighbors γ and the lattice constant a is chosen to be units. The flow J corresponding to $\vec{\psi}_{K+}$ in (26) is $J = m \sin(\eta - k_2 + 2\pi/3) + n \sin(-\eta + k_1 + 2\pi/3)$, where the first term comes from the m bonds, $1 \leq i \leq m$, and the second term comes from the other n bonds. Here $k_i = \vec{k} \cdot \vec{e}_i$ and η is the angle of \vec{R}_7 with respect to x axis, i.e., $(\cos(\eta), \sin(\eta)) = (\sqrt{3}(m+n)/(2R_7), (n-m)/(2R_7))$ and $R_7 = \sqrt{m^2 + n^2 + mn}$. By developing about k_i to the first order and using the boundary condition $mk_1 + nk_2 = 0$, the flow J is represented as

$$J = R_7 - \frac{\sqrt{3}k_1}{2R_7} m(n+m) + O(k_1^2) + O(k_2^2) . \quad (57)$$

The absolute value of the second term in (57) is less than $\sqrt{3}\pi R_7/R_5$, since the energy region where the channel number is kept to two, i.e., $kR_5 \leq 2\pi$, is considered now. It can be deduced from it that the flow is the almost constant value, R_7 , when $R_5 \gg \sqrt{3}\pi$. On the other hands, the value of $|\bar{\alpha}_{7+}|^2$ obtained by substituting F 's in eq.(41) with those of eq.(26) for $\bar{\psi}_{K+}$ is also R_7 . Therefore the normalization factor in eq.(41) is correct. The normalization factor of Ref.¹⁶ and Ref.¹⁸ is different from it by a factor $\sqrt{2}$. This difference does not change the transmission rate, but when ratio between the wave function in the tube parts and that in the junction part is considered, the normalization factor in eq.(41) have to be used.

- ¹ M. Bockrath, D. H. Cobden, P. L. McEuen, N.G. Chopra, A. Zettl, A. Thess and R. E. Smalley, *Science* **275**, 1922 (1997), T. W. Ebbesen, H. J. Lezec, H. Hiura, J. W. Bennett, H. F. Ghaemi and T. Thio, *Nature* **382**, 54 (1996), A. Yu. Kasumov, I. I. Khodos, P. M. Ajayan and C. Colliex, *Europhys. Lett.* **34**, 429 (1996), L. Langer, V. Bayot, E. Grivei, J. -P. Issi, C. Van Haesendonck and Y. Bruynseraede, *Phys. Rev. Lett.* **76**, 479 (1996), S. J. Tans, M. H. Devoret, H. Dai, A. Thess, R. E. Smalley, L. J. Geerlings and C. dekker, *Nature(London)* **386**, 474 (1997), S. Frank, P. Poncharal, Z. L. Wang and W. A. de Heer, *Science* **280** 1774 (1998).
- ² S.Iijima, *Nature (London)* **354**, 56 (1991).
- ³ R. Saito, M. Fujita, G. Dresselhaus and M. S. Dresselhaus, *Phys. Rev. B* **46**, 1804 (1992) , J.W.Mintmire, B. I. Dunlap and C. T. White, *Phys. Rev. Lett.* **68**, 631 (1992), N. Hamada S. Sawada and A. Oshiyama, *ibid.* **68**, 1579 (1992).
- ⁴ M. S. Dresselhaus, G. Dresselhaus and R. Saito, *Solid State Commun.* **84**, 201(1992).
- ⁵ M. P. Anantram and T. R. Govindan, *Phys. Rev. B* **58**, 4882 (1998), T. Kostyrko, M. Bartkowiak and G. D. Mahan, *ibid.* **59** 3241 (1999).
- ⁶ T. Ando and T. Nakanishi, *J. Phys. Soc. Jpn.* **67** 1704 (1998).
- ⁷ S. Iijima, T. Ichihashi and Y. Ando, *Nature(London)* **356**, 776 (1992).
- ⁸ R. Tamura and M. Tsukada, *Phys. Rev. B* **55**, 4991 (1997).
- ⁹ R. Tamura and M. Tsukada, *Z. Phys. D* **40**, 432 (1997).
- ¹⁰ R. Saito, G. Dresselhaus, and M. S. Dresselhaus, *Phys. Rev. B* **53**, 2044 (1996).
- ¹¹ L. Chico, V. H. Crespi, L. X. Benedict, S. G. Louie and M. L. Cohen, *Phys. Rev. Lett.* **76**, 971 (1996), L. Chico, L. X. Benedict, S. G. Louie and M. L. Cohen, *Phys. Rev. B* **54**, 2600 (1996), T. Nakanishi and T. Ando, *J. Phys. Soc. Jpn.* **66**, 2973 (1997), J. -C. Charlier, T. W. Ebbesen and Ph. Lambin, *Phys. Rev. B* **53**, 11108 (1996), M. Menon and D. Srivastava, *Phys. Rev. Lett.* **79**, 4453 (1997), V. Meunier, L. Henrard, and Ph. Lambin, *Phys. Rev. B* **57** 2586.
- ¹² R. Tamura and M. Tsukada, *Phys. Rev. B* **49**, 7697 (1994).
- ¹³ R. Tamura, K. Akagi, M. Tsukada, S. Itoh and S. Ihara, *Phys. Rev. B* **56**, 1404 (1997), S. Ihara, S. Itoh, K. Akagi, R. Tamura and M. Tsukada, *Phys. Rev. B* **54**, 14713 (1996).
- ¹⁴ R. Tamura and M. Tsukada, *Phys. Rev. B* **52**, 6015 (1995), D. L. Carroll, P. Redlich, P. M. Ajayan, J. C. Charlier, X. Blase, A. De Vita and R. Car, *Phys. Rev. Lett* **78**, 2811 (1997).
- ¹⁵ H. Matsumura and T. Ando, *J. Phys. Soc. Jpn.* **67** 3542 (1998).
- ¹⁶ R. Tamura and M. Tsukada, *Phys. Rev. B* **58** 8120 (1998).
- ¹⁷ K. Akagi, R. Tamura, M. Tsukada, S. Itoh and S. Ihara, *Phys. Rev. B* **53**, 2114 (1996), K. Akagi, R. Tamura, M. Tsukada, S. Itoh and S. Ihara, *Phys. Rev. Lett.* **74**, 2307 (1995).
- ¹⁸ R. Tamura and M. Tsukada, *J. Phys. Soc. Jpn.*, in press.
- ¹⁹ H. Ajiki and T. Ando, *J. Phys. Soc. Jpn.* **65** 2976 (1996).
- ²⁰ D. P. DiVincenzo and E. J. Mele, *Phys. Rev. B* **29** 1685 (1984).
- ²¹ Though the sign $\epsilon/|\epsilon|$ is absent in Ref.¹⁶, it is necessary. This difference does not change the transmission rate, but it must be considered when the wave function is calculated.
- ²² When the probability flow of the wave function $\sum(x_i\psi_i + y_i\psi_i^*)$ becomes $\sum(|x_i|^2 - |y_i|^2)v_i$ where cross terms like x^*y and y^*x do not appear, we call $\{\psi_i\}$ is "orthogonalized". Here "orthogonalized" does not mean that for usual inner products of the wave functions $\int dV\psi_i^*(x)\psi_j(x)$, but means that for the probability flow, $\int dS\hat{J}(\psi_i, \psi_j)$, where \hat{J} is the operator of the probability flow defined in Appendix and $\int dS$ means the integration about the cross section of the system. Furthermore ψ 's are normalized so that v_i becomes a constant independent of i . Such a set of "orthonormalized" wavefunctions $\{\psi_i\}$, generally speaking, are not orthonormal in a usual meaning, i.e., $\int dV\psi_i^*(x)\psi_j(x) \neq \delta_{ij}$.
- ²³ Note that in general problems, orthogonality of the incident waves and that of the transmitted waves hold in the same time only when the incident waves are chosen to be 'eigen channels' discussed in Ref.²⁴.
- ²⁴ M. Brandbyge, M. S. Sorensen, and K. W. Jacobsen, *Phys. Rev. B* **56**, 14956 (1997).

FIG. 1. The development map showing the bond network of the (2,2)-(2,5) junction. The filled circle at the bottom and the open circle at the top in each bar indicate an identical atom. To form the junction, the development map is rolled up so that the filled circle and the open circle coincide with each other in each bar. The solid lines and the dashed lines represent the bonds within the bar and those connecting the neighboring bars, respectively. The points $P_5(=Q_5)$, $P_7(=Q_7)$ and O are the centers of the pentagonal defect, that of the heptagonal defects and the origin of the coordinate, respectively, which are shown also in Fig. 3. The two sets of the translation vectors, $\{\vec{e}_1, \vec{e}_2\}$ and $\{\vec{e}'_1, \vec{e}'_2\}$, and corresponding sets of orthogonal vectors $\{\vec{e}_x, \vec{e}_y\}$ and $\{\vec{e}_{x'}, \vec{e}_{y'}\}$ are shown. Note that definition of sublattices A and B are changed between the two sets.

FIG. 2. Notation to represent the amplitudes of the wave function. It is illustrated with the first bar and the second bar in Fig.1. The site in the j 'th bar can be classified to the two groups according to whether it connects with the right $(j+1)$ 'th bar or with the left $(j-1)$ 'th bar. The former and the latter are denoted by $r_{j,i}$ (closed triangles) and $l_{j,i}$ (closed squares), respectively, when the corresponding site has the bond i , which connects the neighboring bars and is numbered from the bottom to the top.

FIG. 3. Development map of the nanotube junctions. The lines 'E₇P₇P₅E₅' are connected and become identical with the lines 'F₇Q₇Q₅F₅', respectively. The rectangles 'E₇P₇Q₇F₇' and 'P₅E₅F₅Q₅' form the thinner tube and the thicker tube, respectively. The triangle 'OP₇P₅' is the same as the 'OQ₇Q₅' rotated by 60 degrees. The quadrilateral 'P₇P₅Q₅Q₇' forms a junction part with a shape of a part of a cone. A heptagonal defect and a pentagonal defect are introduced at P₇(=Q₇) and P₅(=Q₅), respectively. The direction of the circumferences of the tubes in the development map is represented by their angles η_5 and η_7 measured anti-clockwise with respect to the x axis which is defined in Fig. 1. The angle between the axes of the two tubes, ϕ , is defined as $\phi = \eta_7 - \eta_5$.

FIG. 4. Transmission rates per channel, T , as a function of the energy. The transmission rate calculated by eq.(51) are shown by the solid lines, and those calculated by the tight binding model are shown by the dotted line for the (10,10)-(13,13) junction and by the dashed line for the (3,3)-(13,13) junction. The considered energy region is $|E| < E_c$ where the channel number is kept to two in both the tube parts. The threshold energy E_c for the effective mass theory is about $0.242|\gamma|$ and that for the tight binding model is about $0.239|\gamma|$, where $\gamma < 0$ is the hopping integral. One can easily see the agreement between the two methods is fairly good.

FIG. 5. Schematic development maps representing the relation between the radial norm Φ and the transmission rate T . The thicker tube and the region CC'D'D are common in both the development maps

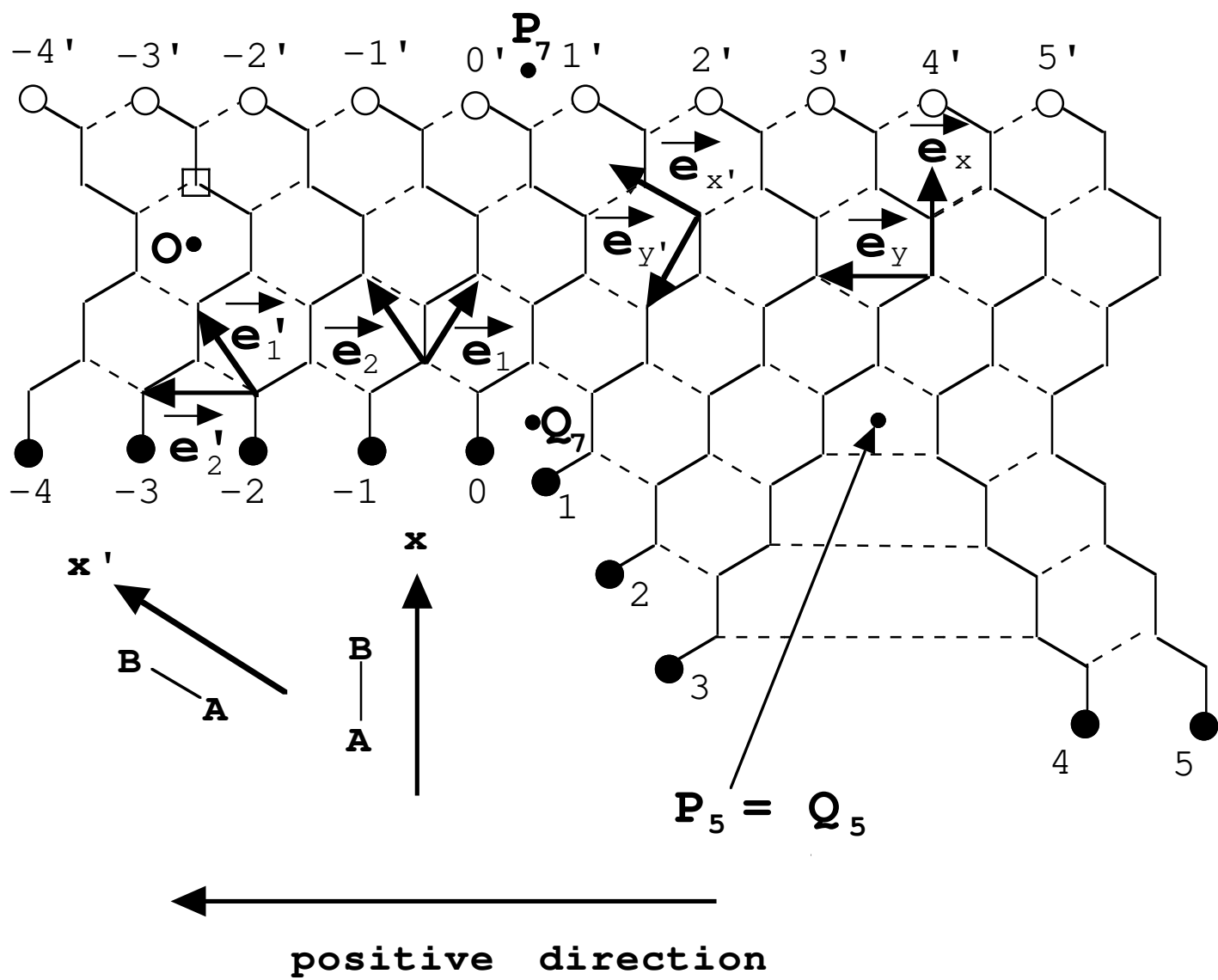
FIG. 6. Inverse of the radial norm for the positive incidence direction defined by $2/(\Phi(kR_7, kR_5) + 1)$, and that for the negative incidence direction $2/(\Phi(kR_5, kR_7) + 1)$ are shown by the dashed lines and the dotted lines, respectively. Here the radial norm Φ is defined in eq.(55). Values of R_7/R_5 are 0.1, 0.3, 0.5, 0.7, and 0.9, which are attached to the corresponding lines. The transmission rate per channel calculated by eq.(51) is shown by the solid lines. It can be seen that the radial norm gives a good estimated value of the transmission rate. The horizontal axis is the energy normalized by E_c . Here $|E| < E_c$ represents the energy region where the channel number is kept to two in both the tube parts.

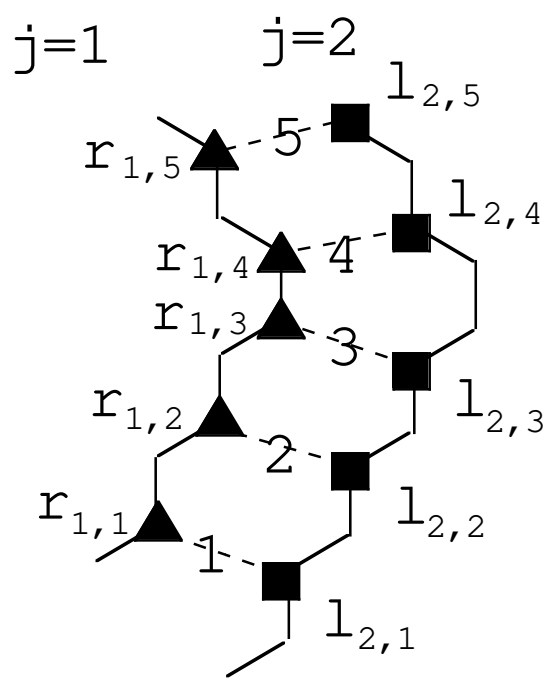
FIG. 7. Radial norm for the negative incidence direction, i.e., $\Phi(kR_5, kr)$ is shown as a function of r/R_5 for five energies, $kR_5/(2\pi) = E/E_c = 0.1, 0.3, 0.5, 0.65, 0.8$ and 1.0. Here Φ is defined by eq.(55). The values of E/E_c are attached to the corresponding lines. Both the axes are represented with log scale. Inset shows the regions of the parameter space, I, II, III and IV, which are used in the discussion in the text.

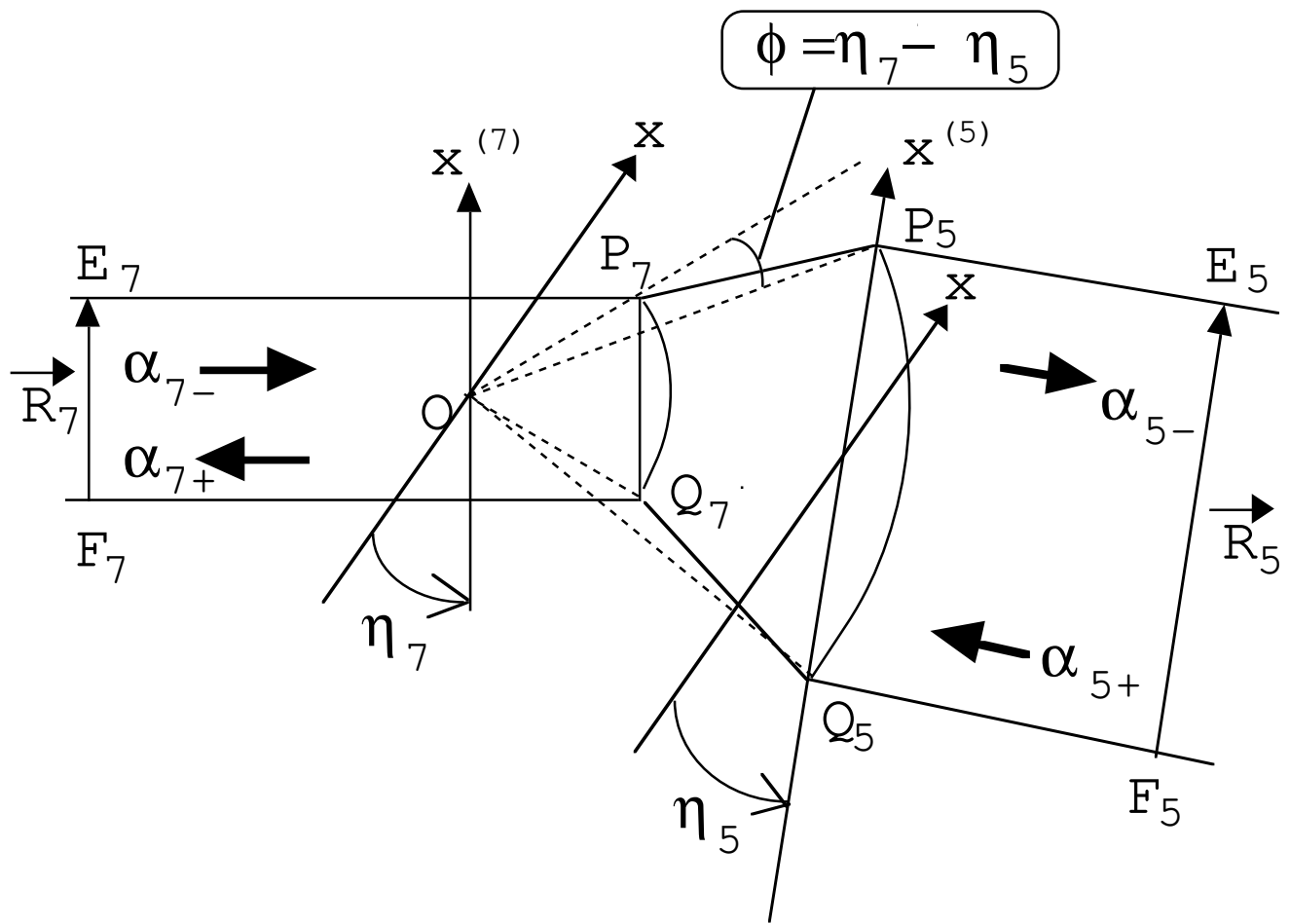
FIG. 8. Comparison between the wave functions $|c_{j,i}^{(k)}|^2$ calculated by the tight binding model, and Ψ defined by eqs.(53) and (54); It shows $(|c_{j,i}^{(1)}|^2 + |c_{j,i}^{(2)}|^2)/(T\Psi)$ as a function of radial distance, r , (a) for the (3,3)-(13,13) junction and (b) for the (10,10)-(13,13) junction. They are shown for $j = 1, 2, \dots, l_1$. The energy is $E = -0.05|\gamma|$. Here $|c_{j,i}^{(k)}|^2$ is caused by the incident waves with positive direction, $\tilde{\psi}_{k+}^R$. Here $1/T = |h_+|^2$ defined by eq.(49) is used for the normalization. The vertical axis is represented with log scale. Data at the pentagon and at the heptagon are shown by the closed diamonds.

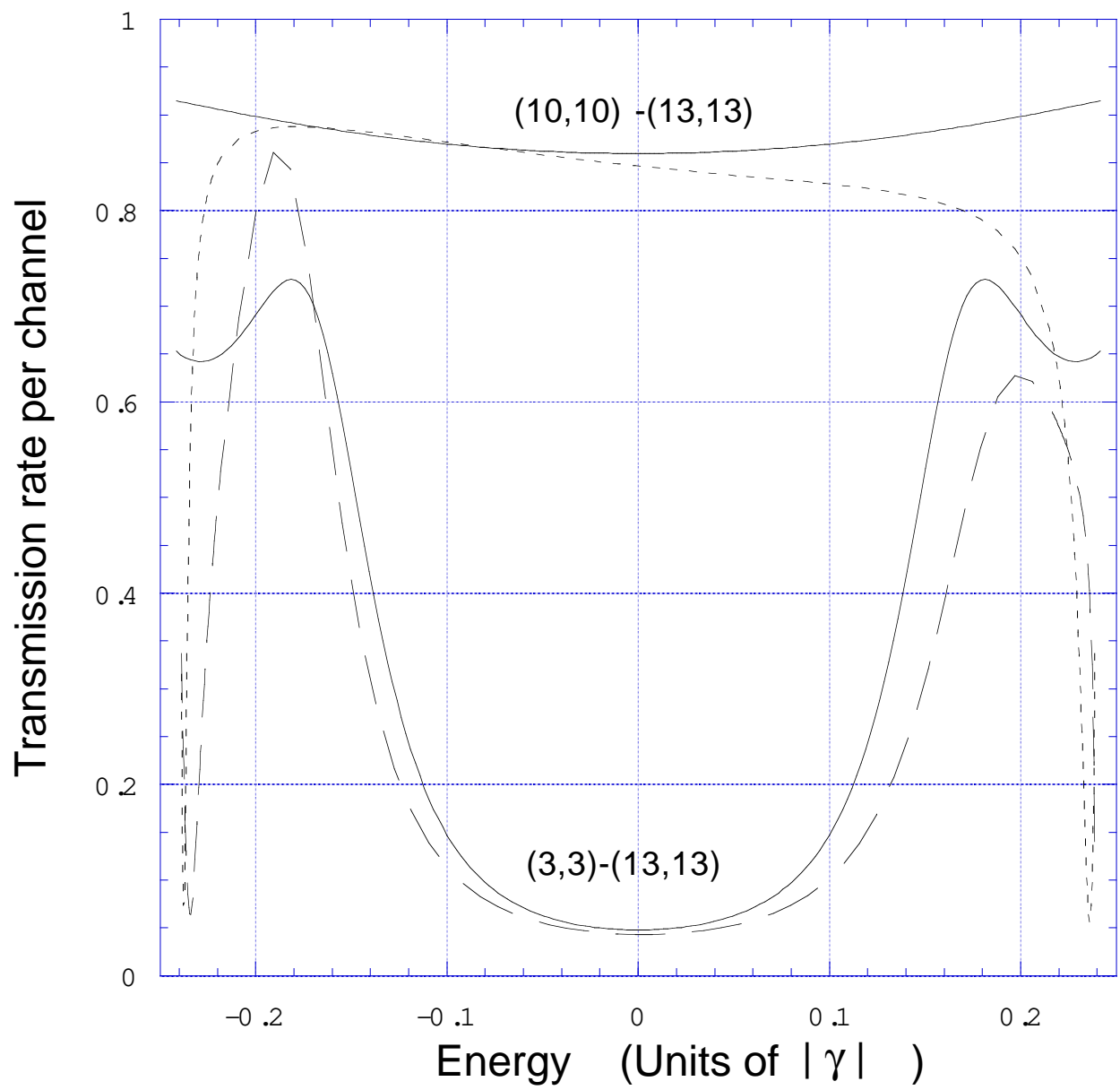
FIG. 9. Norm of the wave function of each bar, $|\vec{c}_j|^2$, of the (3,3)-(13,13) junction (a) for $E = \pm 0.2|\gamma|$ and (b) for $E = \pm 0.23|\gamma|$. The horizontal axis represents the position of the bar j shown in Fig.1. The incidence direction is positive, i.e., from the right to the left in this figure. The dotted lines with closed symbols and the solid lines with open symbols correspond to those calculated by eq.(13) and those calculated by eqs.(53) and (54), respectively. The diamonds and the squares correspond to the positive energy and the negative energy, respectively.

FIG. 10. The localization strength for the θ direction (a) at the pentagon and (b) at the heptagon as a function of the energy. The incidence direction is positive. The solid lines and the dashed lines correspond to the (10,10)-(13,13) junction and the (3,3)-(13,13) junction, respectively.

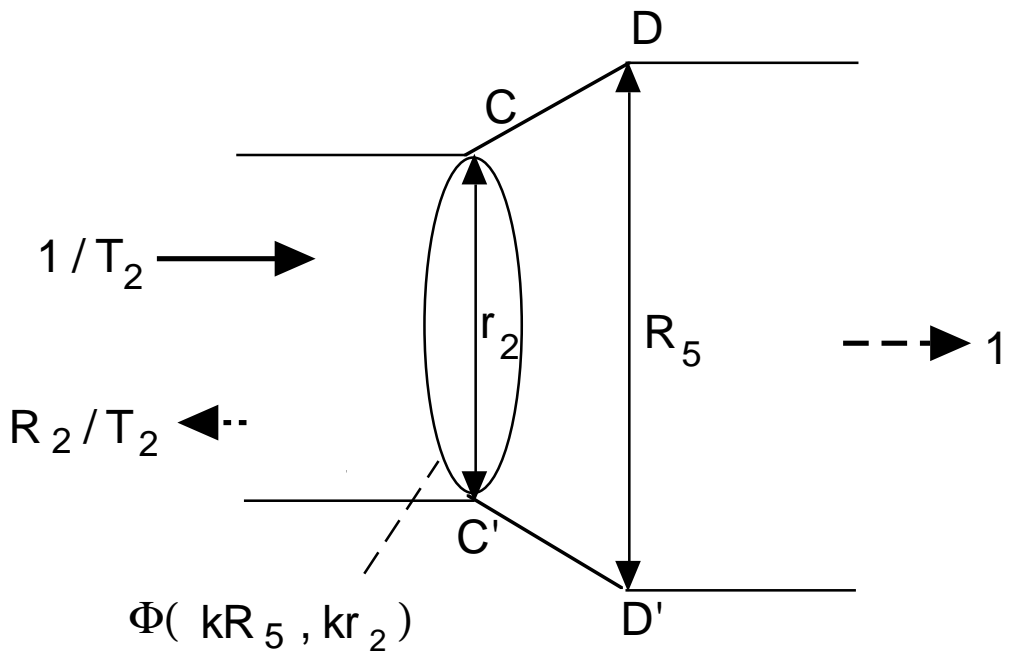
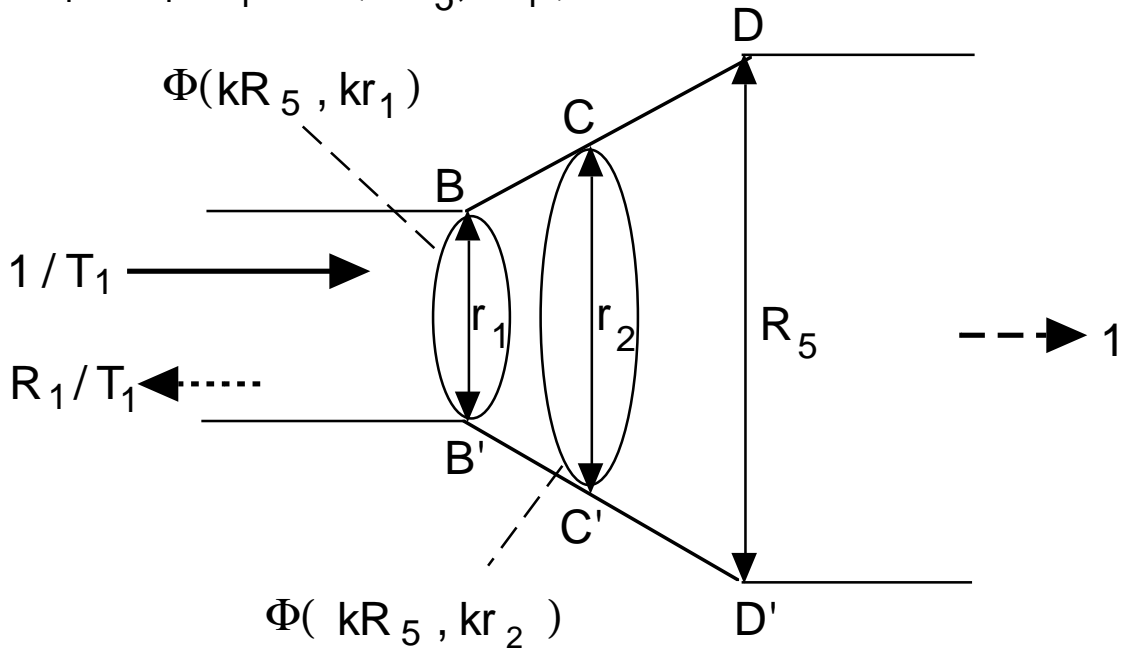








$$1/T_1 + R_1/T_1 = \Phi(kR_5, kr_1)$$



$$1/T_2 + R_2/T_2 = \Phi(kR_5, kr_2)$$

